Progress In Electromagnetics Research C, Vol. 167, 205–217, 2026

PIER C

(Received 2 November 2025, Accepted 8 December 2025, Scheduled 22 March 2026)

Complex Vector-Based PI Parameter Optimization for PMSM Systems with LCL Filter

Xintian Liu, Yunyue Sun, Xinxin Zheng*, Yao He, Yanan Zhou, and Lin He

College of Automotive and Traffic Engineering, Hefei University of Technology, Hefei 230009, China

ABSTRACT: To address the challenge of achieving both steady-state accuracy and fast dynamic response in permanent magnet synchronous motor (PMSM) systems equipped with LCL filters, this paper proposes a complex vector PI controller optimization method. The proposed approach extends the conventional real-axis PI control to the complex domain, enabling unified modeling of current decoupling and harmonic suppression. Based on this formulation, the response surface methodology (RSM) is employed to optimize the controller parameters. A quadratic response model is established through the design of experiments (DOE), with steady-state error, dynamic overshoot, and harmonic suppression indices defined as optimization objectives to obtain the optimal parameter set. The core contribution of this work is the integration of a frequency-domain complex-vector model with a systematic multi-objective optimization framework using Response Surface Methodology (RSM) and Generalized Reduced Gradient (GRG) algorithms. This approach addresses the inherent coupling and resonance issues in LCL-filtered PMSM systems. Quantitative experimental results demonstrate that, compared with conventional tuning methods, the proposed strategy reduces the current settling time by 47.6% and suppresses torque overshoot by 92.8%, thereby achieving a superior balance between fast transient response and steady-state accuracy.

1. INTRODUCTION

Driven by the global energy transition and the “dual carbon” targets, electric vehicles (EVs) have gradually become an important alternative to traditional fuel-powered vehicles [1]. Among the three key components of EV powertrains — motor, motor controller, and battery — the drive motor system plays a central role, as its performance directly determines the vehicle’s power, efficiency, and comfort [2]. Permanent magnet synchronous motors (PMSMs), owing to their high power density, high efficiency, and excellent speed regulation capability, are widely adopted in main traction systems [8]. The maturity of vector control (VC) technology has further enabled high-performance control of PMSMs [9].

However, the essence of VC lies in transforming the original three-phase AC quantities into DC quantities through coordinate transformation for control purposes. In the synchronous rotating reference frame (SRF), new coupling relationships emerge between the current variables, particularly cross-interference between the d-axis and q-axis currents, which severely affects both the dynamic response and steady-state performance of the motor system [9]. In practical engineering, inductor-capacitor-inductor (LCL) filters are commonly inserted between the inverter and the motor to mitigate electromagnetic interference and suppress harmonic currents at the motor terminals [3]. Although LCL filters provide excellent high-frequency attenuation, they also significantly alter the system dynamics, introducing higher-order dynamics and stronger dq-axis coupling, thereby greatly increasing the difficulty of current loop control [4].

Therefore, on the basis of existing vector control structures, optimizing controller parameters to enhance system dynamic response and disturbance rejection, while maintaining effective decoupling, holds both high engineering value and theoretical significance [12]. Currently, for current loop control under LCL filters, various decoupling strategies have been proposed, including feedforward compensation, state feedback, and complex-vector-based decoupling [17]. Among them, the state feedback approach relies heavily on precise system modeling, making it sensitive to parameter variations and nonlinear disturbances, and prone to instability [18]. Traditional complex-coefficient proportional-integral (PI) controllers can achieve partial dq-axis decoupling but still suffer from slow response, significant residual coupling, and limited design flexibility in systems with LCL filters [14]. Multi-constraint complex PI controllers improve decoupling performance through techniques such as pole-zero cancellation, but they still fall short in balancing bandwidth optimization and dynamic performance constraints [15].

On the other hand, most existing studies emphasize innovations in controller structure, while relatively few address parameter optimization itself — particularly with respect to comprehensive multi-objective performance criteria, such as bandwidth, phase margin, and dq-axis symmetry [8, 10, 15, 16, 25].

In the international context, significant advancements have been made in addressing the coupling and resonance issues of LCL-filtered PMSM drives. The foundational work by Harnefors et al. [24] established passivity-based design criteria to prevent electrical resonance instability, providing a rigorous theoretical basis for system robustness. Building on robust con-

---

[*] Corresponding author: Xinxin Zheng (xinxin.zheng@hfut.edu.cn).

doi:10.2528/PIERC25110201

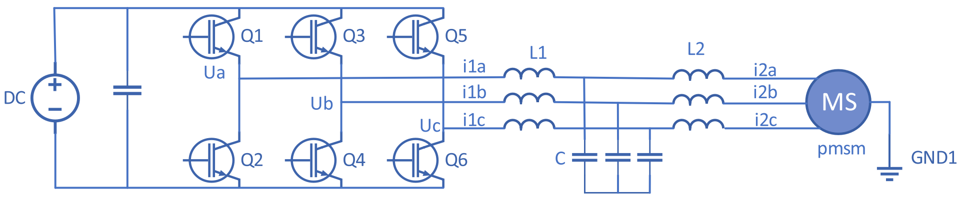

FIGURE 1. Topology of the LCL-type motor inverter main circuit.

trol theories, Cheng et al. [23] recently proposed a fast current control strategy for LCL-equipped high-speed PMSMs to mitigate delay effects and ensure stability. In the specific domain of complex-vector control, Lyu and Wu [21] developed a decoupling and resonance suppression scheme in the synchronous complex-vector frame, effectively analyzing the cross-coupling effects. Regarding systematic optimization, Du et al. [22] demonstrated the efficacy of surrogate model-based optimization methodologies for PMSM design under complex operating conditions.

However, a critical gap remains in the existing literature: While studies like [23] and [24] focus heavily on stability boundaries and robustness, and [21] establishes the control architecture, they often rely on analytical parameter tuning (e.g., pole placement), which requires precise model knowledge. Conversely, optimization studies like [22] primarily focus on motor structural design rather than the dynamic tuning of complex LCL control parameters. Therefore, this paper proposes a unified framework that integrates the complex-vector modeling (inspired by [21]) with an RSM-based multi-objective optimization (similar to the methodology in [22]), thereby bridging the gap between theoretical decoupling and practical performance tuning.

The main contributions and novelties of this paper are summarized as follows:

(1) A complex-vector frequency-domain model is established to explicitly characterize the cross-coupling effects introduced by LCL filters, providing a theoretical basis for precise decoupling control.

(2) A systematic parameter tuning framework combining Central Composite Design (CCD) and the GRG algorithm is proposed to solve the multi-objective conflict between settling time and overshoot.

(3) Theoretical analysis and experimental validation quantify the performance improvements, confirming that the optimized controller significantly enhances dynamic bandwidth and robustness compared to traditional methods [13].

This work not only provides theoretical guidance for controller tuning in EV drive systems with LCL filters but also contributes to the design of control strategies for future high-power, high-performance motor systems [5, 6].

2. SYSTEM ANALYSIS AND COMPLEX-VECTOR CONTROL STRATEGY

2.1. System Modeling

To achieve high-performance control of permanent magnet synchronous motors (PMSMs) in electric vehicle (EV) drive systems, this paper proposes a complex-vector current control strategy based on an LCL filter [7]. Taking the stator current as the control target, the strategy establishes a complex-vector model in the synchronous rotating reference frame (dq-axis) [20], thereby overcoming the coupling issues introduced by the higher-order dynamics of the LCL filter in conventional control methods [11]. This approach significantly improves current response speed and dynamic performance.

The overall structure of the control system is illustrated in Figure 1. It consists of a three-phase voltage-source PWM inverter, an LCL filter, a PMSM, and feedback loops. The core modules of the system include an outer-loop speed controller, an inner-loop current controller, coordinate transformation modules, a space vector pulse width modulation (SVPWM) module, and the LCL filtering stage. The outer-loop speed controller employs a PI regulator, which dynamically adjusts the q-axis current reference according to the speed error [19]. The control equation can be expressed as:

$$i_q^* = K_{p\omega}(\omega^* - \omega) + K_{i\omega}\int(\omega^* - \omega)dt \tag{1}$$

Here, ω^* denotes the reference speed, while $K_{p\omega}$ and $K_{i\omega}$ represent the proportional and integral gains, respectively. The inner-loop current controller adopts a complex-coefficient PI algorithm to achieve independent closed-loop control of the dq-axis currents. In combination with coordinate transformation and SVPWM modulation techniques, this ensures accurate current tracking.

Figure 1 illustrates the topology of the LCL-type motor inverter main circuit. In this configuration, U_{dc} is the DC bus voltage; u_a, u_b, u_c are the inverter output phase voltages; L_1 and L_2 represent the inverter-side and motor-side inductances, respectively; C is the filter capacitance; i_{1a}, i_{1b}, i_{1c} are the inverter-side currents; and i_{2a}, i_{2b}, i_{2c} are the motor-side currents.

The LCL filter, serving as a critical interface between the inverter and the motor, consists of the inverter-side inductor L_1, filter capacitor C_f, and motor-side inductor L_2. Its transfer function describing the relationship between the inverter output voltage vector and the motor-side current vector in the synchronous rotating reference frame can be expressed as:

$$G_{\mathrm{LCL}}(s) = \frac{1 + R_f C_f s}{L_1 L_2 C_f s^3 + (L_1 + L_2) R_f C_f s^2 + (L_1 + L_2) s} \tag{2}$$

In this derivation, to establish a tractable linear model for controller design, nonlinear factors, such as inverter dead-time effects and sampling delays, are neglected [25]. However, the potential impact of these unmodeled dynamics is mitigated through the robustness margins enforced in the subsequent parameter optimization process.

This third-order system, while effective in suppressing high-frequency harmonics, introduces significant dynamic coupling and resonance risks. Specifically, the asymmetric terms in the capacitor current feedback path make it difficult for conventional real-coefficient PI controllers to achieve complete decoupling. Moreover, small deviations in filter parameters L_1, L_2, and C_f can substantially impact system stability and bandwidth.

2.2. Complex Vector Control Strategy

To address these issues, this study proposes a multi-constrained control strategy based on complex-vector modeling. First, the dq-axis currents are combined into a complex vector form $i_{dq} = i_d + ji_q$, transforming the dual-input dual-output (MIMO) system into a single-input single-output (SISO) complex-variable model. On this basis, a complex-coefficient PI controller is designed, whose transfer function is given by:

$$G_{\mathrm{PI}}(s) = K_p + \frac{K_i}{s} \tag{3}$$

where $K_p = K_{p1} + jK_{p2}$ and $K_i = K_{i1} + jK_{i2}$ are complex coefficients. By employing the principle of pole-zero cancellation, the controller is able to compensate for the complex poles introduced by the LCL filter, while symmetry constraints are used to optimize the frequency response characteristics in both positive and negative domains.

The transfer function of the complex-coefficient PI controller can be further expressed as:

$$G_{\mathrm{PI}}(s) = G_{\mathrm{PIre}}(s) + jG_{\mathrm{PIim}}(s) \tag{4}$$

As illustrated in Figure 2, the controller input signals are Δi_d and Δi_q, and the output signals are e_d and e_q. Since the dq-axis outputs are inherently coupled, the complex-coefficient PI controller leverages its intrinsic coupling characteristics to cancel the poles introduced by the filter inductances.

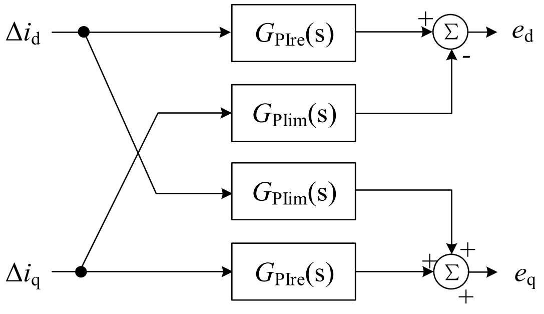

FIGURE 2. Block diagram of the complex-coefficient PI controller.

The workflow of the control system can be summarized as follows: the encoder provides real-time feedback of the rotor position θ and speed ω. The outer-loop PI controller generates the q-axis current reference i_q^*. The three-phase currents are transformed into dq-axis currents i_d and i_q through Clarke and Park transformations. These actual currents are then compared with the reference values and fed into the complex-coefficient PI controller. The controller outputs dq-axis voltage commands, which are converted into $\alpha\beta$ voltages via the inverse Park transformation. Subsequently, the SVPWM module modulates these signals into six PWM pulses to drive the inverter. The inverter outputs are filtered through the LCL filter to suppress high-frequency harmonics before being applied to the motor, ultimately achieving high-precision current tracking. To suppress speed-dependent coupling terms, a complex-vector decoupling factor $\Delta = \omega_e(L_1 + L_2)$ is introduced at the controller output, effectively compensating for cross-coupling during dynamic processes.

2.3. Comparison with Traditional dq-PI Control

To clarify the theoretical advantages of the proposed method, it is essential to distinguish it from the traditional control structure. The traditional dq-PI control approach treats the d-axis and q-axis as two separate channels, employing two independent real-valued PI controllers. To handle the coupling caused by inductance and motor rotation, explicit feedforward decoupling terms are typically added to the controller output. However, this method relies heavily on accurate parameter knowledge and often fails to effectively decouple the frequency-dependent cross-coupling introduced by the LCL filter resonance.

In contrast, the proposed strategy treats the current vector as a single complex variable. The controller employs complex-valued gains, where the real parts correspond to the bandwidth and zero locations of the main loops, while the imaginary parts inherently provide rotationally invariant decoupling. Unlike static feedforward terms, these complex coefficients dynamically compensate for the cross-coupling effects across the entire frequency range. This characteristic makes the complex-vector PI controller particularly effective for managing the high-order dynamics of LCL filters. Therefore, optimizing the complex PI parameters is mathematically equivalent to simultaneously tuning the main loop gains and the dynamic decoupling gains in a unified framework.

2.4. Frequency Domain Analysis

Figure 3 illustrates the influence of each parameter of the complex-coefficient PI controller on its frequency-domain characteristics. The controller parameters are derived based on the inverter-side current feedback model, denoted as $G_{\mathrm{plant,inv}}(s)$. When the LCL filter parameters exhibit a + 10% deviation, the parameter variation ranges are as follows: $\mathrm{Re}(K_p) \in [3.2, 4.8]$, $\mathrm{Im}(K_p) \in [-0.5, 0.5]$, $\mathrm{Re}(K_i) \in [477.1, 739.4]$, and $\mathrm{Im}(K_i) \in [1001.7, 1405.4]$.

Figure 3(a) shows the frequency response when only $\mathrm{Re}(K_p)$ is varied. $\mathrm{Re}(K_p)$ primarily affects the attenuation magnitude during pole-zero cancellation and the phase shift at high frequencies. A larger $\mathrm{Re}(K_p)$ results in greater attenuation and smaller phase deviation.

Figure 3(b) shows the response when only $\mathrm{Im}(K_p)$ is varied. $\mathrm{Im}(K_p)$ mainly affects the zero location and attenuation magnitude. As $\mathrm{Im}(K_p)$ increases, the zero shifts leftward, and the attenuation magnitude increases.

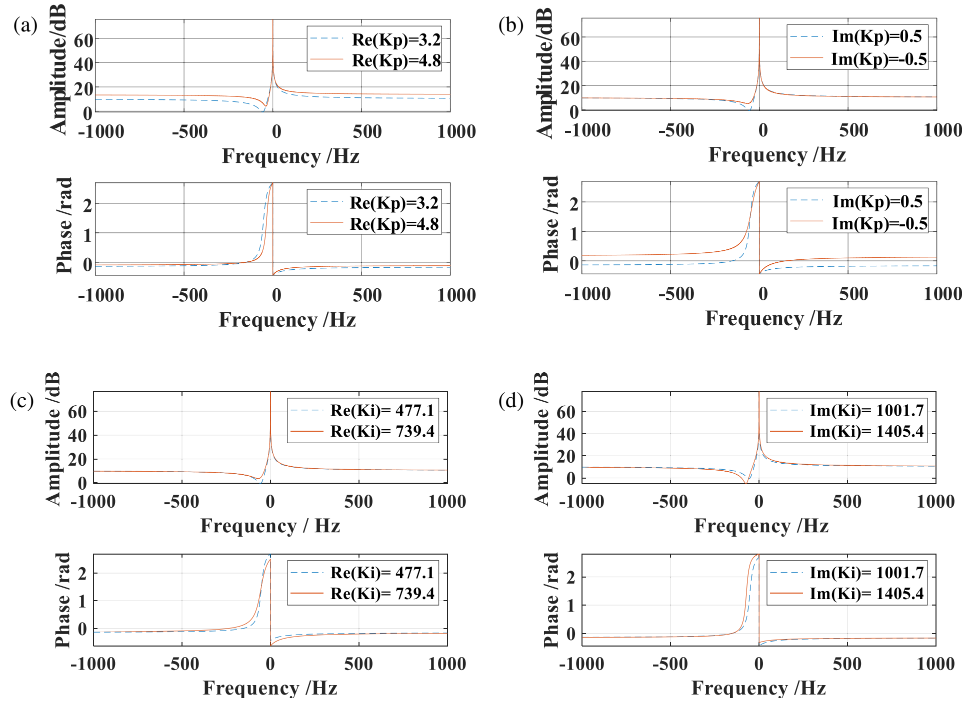

FIGURE 3. Influence of complex-coefficient PI controller parameters on frequency-domain characteristics.

Figure 3(c) shows the response when only $\mathrm{Re}(K_i)$ is varied. $\mathrm{Re}(K_i)$ influences the zero location and attenuation magnitude, with a trend consistent with that in Figure 3(b).

Figure 3(d) shows the response when only $\mathrm{Im}(K_i)$ is varied. $\mathrm{Im}(K_i)$ affects the attenuation magnitude and phase shift near the zero. A larger $\mathrm{Im}(K_i)$ leads to smaller attenuation but greater phase deviation.

From Figure 3, it can be observed that within the parameter variation ranges corresponding to $a+10\%$ deviation of the LCL filter parameters, the frequency response curves exhibit only minor changes. For controller parameters obtained based on the motor-side current feedback model, denoted as $G_{\text{plant,mot}}(s)$, the influence trends are identical since the controller transfer function shares the same form. Therefore, their response curves are not repeated here.

The parameter deviations of a complex-coefficient controller significantly affect the system's dynamic performance, mainly in three aspects: first, fluctuations in both the real and imaginary parts of the parameters cause shifts in the locations of the controller's zeros and poles, directly impacting system stability; second, parameter variations alter the frequency-domain response characteristics, especially phase margin and magnitude curves, thereby affecting dynamic response quality; finally, in multivariable coupled systems, such effects can be amplified through the transfer function matrix, further reducing system robustness. Even within $a \pm 10\%$ deviation range of LCL filter parameters, the controller's performance indices still exhibit considerable fluctuations. Therefore, parameter optimization of the complex-coefficient controller is particularly necessary, not only to ensure stable operation of the system under various operating conditions but also to improve its dynamic response performance.

3. CONTROLLER PARAMETER OPTIMIZATION

3.1. Experimental Design and Modeling

Central Composite Design (CCD) is a commonly used response surface methodology (RSM) that is suitable for building quadratic mathematical models with a limited number of experiments. Its basic concept is to augment a two-level factorial design with additional experimental points located at specific positions, so that the model can capture not only linear and interaction effects but also quadratic effects and curvature variations. CCD generally consists of three types of points: (i) cube points derived from full or fractional factorial designs, used to estimate main and interaction effects; (ii) axial points, also known as star points, positioned at a distance α from the center along each factor axis, introduced to capture quadratic effects; and (iii) center points, typically replicated several times at the mean level of all factors, used to estimate pure error and detect model lack-of-fit. The value of α determines the distance between the axial and center points, and it is usually chosen according to the rotatability principle to ensure uniform prediction accuracy across the design space. Based on the relative positions of the axial points to the experimental region, CCD can be divided into three forms: circumscribed (CCC), inscribed (CCI), and face-centered (CCF), which are respectively suitable for wide ranges, constrained ranges, or limited factor levels. This design method features a flexible arrangement of experimental points, high accuracy in quadratic surface fitting, and relatively fewer experimental runs, making it widely applied in engineering optimization and parameter modeling.

To enhance the dynamic performance of the complex-vector control system with an LCL filter, this study optimizes the PI controller parameters in the d-axis and q-axis current loops.

TABLE 1. Summary of parameter ranges for theoretical analysis, DOE design, and GRG optimization.

Parameter	Symbol	Theoretical Analysis Range (Robustness Check)	DOE Design Levels (Factor Range)	GRG Optimization Search Constraints
P-Gain Real Part	$\mathrm{Re}(K_p)$	[3.2, 4.8]	[3.2, 4.8]	[3.2, 4.8]
P-Gain Imag Part	$\mathrm{Im}(K_p)$	$[-0.5, 0.5]$	$[-0.5, 0.5]$	$[-0.5, 0.5]$
I-Gain Real Part	$\mathrm{Re}(K_i)$	[477.1, 739.4]	[477.1, 1001.7]	[477.1, 1001.7]
I-Gain Imag Part	$\mathrm{Im}(K_i)$	[1001.7, 1405.4]	[739.4, 1405.4]	[739.4, 1405.4]
Filter Inductance	$L_1 L_2$	±10% Deviation	Nominal	Nominal

TABLE 2. Regression coefficients of the equation for t_d.

$\boldsymbol{A_0}$	$\boldsymbol{A_1}$	$\boldsymbol{A_2}$	$\boldsymbol{A_3}$	$\boldsymbol{A_4}$
8	-1.2	6.87	0.0494	-0.0239
$\boldsymbol{A_5}$	$\boldsymbol{A_6}$	$\boldsymbol{A_7}$	$\boldsymbol{A_8}$	$\boldsymbol{A_9}$
0.66	2.01	-0.00036	0.000014	-0.48
$\boldsymbol{A_{10}}$	$\boldsymbol{A_{11}}$	$\boldsymbol{A_{12}}$	$\boldsymbol{A_{13}}$	$\boldsymbol{A_{14}}$
-0.00286	-0.00139	-0.00472	-0.00369	0.000009

TABLE 3. Regression coefficients of the equation for δ_d.

$\boldsymbol{A_0}$	$\boldsymbol{A_1}$	$\boldsymbol{A_2}$	$\boldsymbol{A_3}$	$\boldsymbol{A_4}$
0.96	4.73	-2.324	-0.00638	-0.01153
$\boldsymbol{A_5}$	$\boldsymbol{A_6}$	$\boldsymbol{A_7}$	$\boldsymbol{A_8}$	$\boldsymbol{A_9}$
-0.468	-0.179		0.000012	0.147
$\boldsymbol{A_{10}}$	$\boldsymbol{A_{11}}$	$\boldsymbol{A_{12}}$	$\boldsymbol{A_{13}}$	$\boldsymbol{A_{14}}$
0.001465	0.002435	0.003307	0.001426	0.000001

TABLE 4. Regression coefficients of the equation for t_q.

$\boldsymbol{A_0}$	$\boldsymbol{A_1}$	$\boldsymbol{A_2}$	$\boldsymbol{A_3}$	$\boldsymbol{A_4}$
15.4	29.6	3.1	-0.1379	-0.0218
$\boldsymbol{A_5}$	$\boldsymbol{A_6}$	$\boldsymbol{A_7}$	$\boldsymbol{A_8}$	$\boldsymbol{A_9}$
-2.17	-1.29	0.000081	0.000028	1.85
$\boldsymbol{A_{10}}$	$\boldsymbol{A_{11}}$	$\boldsymbol{A_{12}}$	$\boldsymbol{A_{13}}$	$\boldsymbol{A_{14}}$
-0.00299	-0.00833	0.01779	-0.02699	0.000006

TABLE 5. Regression coefficients of the equation for δ_q.

$\boldsymbol{A_0}$	$\boldsymbol{A_1}$	$\boldsymbol{A_2}$	$\boldsymbol{A_3}$	$\boldsymbol{A_4}$
11.08	-0.65	0.26	-0.00876	-0.00061
$\boldsymbol{A_5}$	$\boldsymbol{A_6}$	$\boldsymbol{A_7}$	$\boldsymbol{A_8}$	$\boldsymbol{A_9}$
0.145	5.45	0.000002	0.000006	-0.122
$\boldsymbol{A_{10}}$	$\boldsymbol{A_{11}}$	$\boldsymbol{A_{12}}$	$\boldsymbol{A_{13}}$	$\boldsymbol{A_{14}}$
0.000856	-0.00161	0.003791	0.001647	0

The optimization process is modeled using Central Composite Design (CCD) within the framework of Design of Experiments (DOE). The input variables are the proportional (K_p) and integral (K_i) coefficients of the d-axis and q-axis PI controllers, i.e., four parameters in total. The outputs are the settling time and overshoot of the active and reactive currents.

First, based on the Simulink simulation model, a motor drive control system is constructed, including the LCL filter, current decoupling, complex-vector control, and SVPWM. Through preliminary analysis of the system's open-loop gain and desired bandwidth, the parameter boundaries were established. To ensure consistency throughout the study, the parameter deviation ranges used in theoretical analysis, the factor levels for the DOE design, and the search constraints for the GRG optimization are summarized in Table 1. Specifically, the DOE exploration ranges were set based on the robustness limits identified in Section 2. Within these ranges, experimental points including center points, axial points, and factorial boundary points are arranged using CCD, reducing the number of experiments while ensuring the fitting accuracy of the response surface model.

Each set of PI parameter values is substituted into the Simulink model for simulation. The settling time (t_d, ms) and maximum overshoot (δ_d, A) of the reactive current response, as well as the settling time (t_q, ms) and maximum overshoot (δ_q, A) of the active current response, are obtained via oscilloscope monitoring as the output responses. The collected experimental data are then input into Minitab software, and a quadratic response surface model is constructed using the RSM module, expressed as follows:

$$y = A_0 + \sum_{i=1}^{n} A_i x_i + \sum_{i=1}^{n} A_{ii} x_i^2 + \sum_{i<j} A_{ij} x_i x_j \qquad (5)$$

where the dependent variable y corresponds to t_d (reactive current settling time), δ_d (reactive current overshoot), t_q (active current settling time), and δ_q (active current overshoot). The independent variables are: $x_1 = \mathrm{Re}(K_p)$ $x_2 = \mathrm{Im}(K_p)$, $x_3 = \mathrm{Re}(K_i)$, $x_4 = \mathrm{Im}(K_i)$. Coefficients A: A_0 is the constant term, A_1–A_4 are linear coefficients, A_5–A_8 are quadratic coefficients, and A_{ij} (e.g., A_9–A_{12}) represent interaction coefficients.

The specific values of each coefficient are shown in Tables 2–5.

To verify the model accuracy, residual plots are drawn in Figure 4.

As shown in Figure 4, the residuals are approximately evenly distributed around zero, with most data points falling within $\pm 3\sigma$ (standard deviation). This indicates that the model exhibits high fitting accuracy and prediction capability. The quadratic response model thus provides a reliable foundation for subsequent optimization analysis.

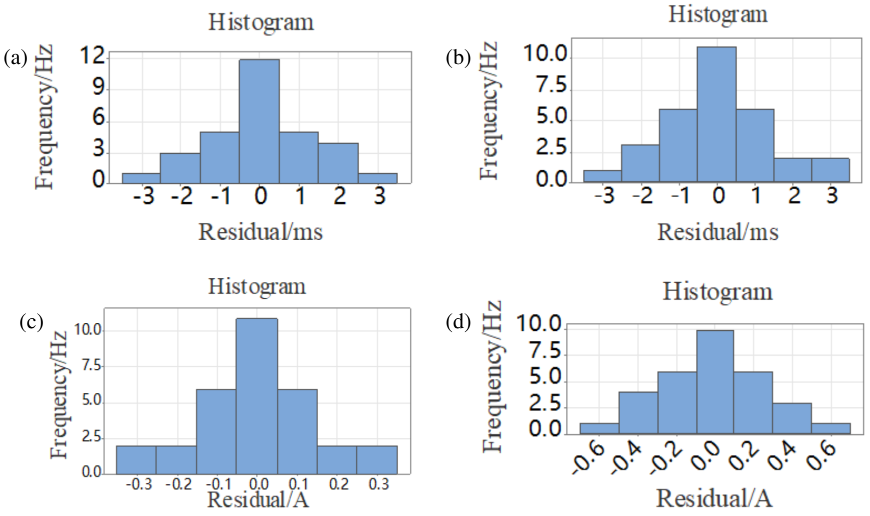

FIGURE 4. Residual plots of active and reactive current settling time and overshoot.

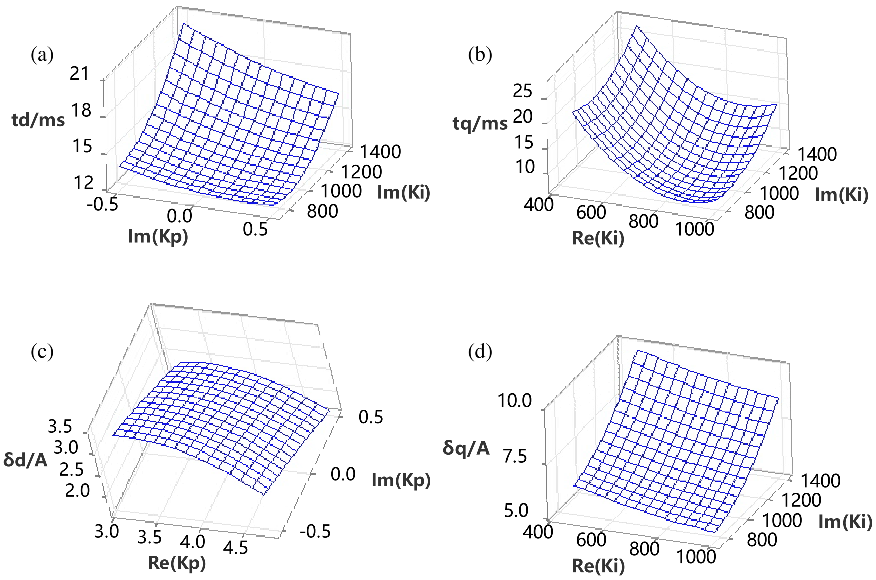

FIGURE 5. Fitted quadratic response surfaces.

Figure 5 illustrates the response surfaces of the four performance indices with respect to PI controller parameters. Specifically, Figure 5(a) shows the response surface of the reactive current settling time t_d with respect to $\mathrm{Im}(K_i)$ and $\mathrm{Im}(K_p)$ (with fixed $\mathrm{Re}(K_p) = 4$, $\mathrm{Re}(K_i) = 739.4$); Figure 5(b) depicts the surface of the active current settling time t_q versus $\mathrm{Im}(K_i)$ and $\mathrm{Re}(K_i)$ (with fixed $\mathrm{Re}(K_p) = 4$, $\mathrm{Im}(K_p) = 0$); Figure 5(c) illustrates the surface of the maximum reactive current overshoot δ_d versus $\mathrm{Im}(K_p)$ and $\mathrm{Re}(K_p)$ (with fixed $\mathrm{Re}(K_i) = 739.4$, $\mathrm{Im}(K_i) = 1072.4$); and Figure 5(d) shows the surface of the maximum active current overshoot δ_q versus $\mathrm{Im}(K_i)$ and $\mathrm{Re}(K_i)$ (with fixed $\mathrm{Re}(K_p) = 4$, $\mathrm{Im}(K_p) = 0$). Overall, these four response surfaces clearly reveal the influence of PI parameter variations on system regulation performance, providing an intuitive basis for defining feasible parameter regions and optimizing solutions.

Under the same conditions as in Figure 5 (PI parameter response surfaces), contour plots of the four performance indices were superimposed to identify feasible parameter regions, as shown in Figure 6. To ensure fast current-loop response while limiting overshoot, the following acceptable ranges were defined: $\delta_q = 2$–8 ms, ensuring controllable active current overshoot for loop stability; $t_q = 3$–15 ms, ensuring dynamic performance; $\delta_d = 2.8$–40 A, limiting reactive current overshoot to avoid excessive load stress; and $t_d = 3$–14 ms, balancing speed and stability.

The white areas in Figure 6 represent PI parameter combinations that simultaneously satisfy all four constraints, forming the initial search domain for optimization. Analysis of these regions shows that δ_q is particularly sensitive to imaginary parameter variations, while t_d and δ_d are more influenced by real parameter variations, and t_q shows coupled sensitivity to combined parameters. This provides a scientific basis for selecting

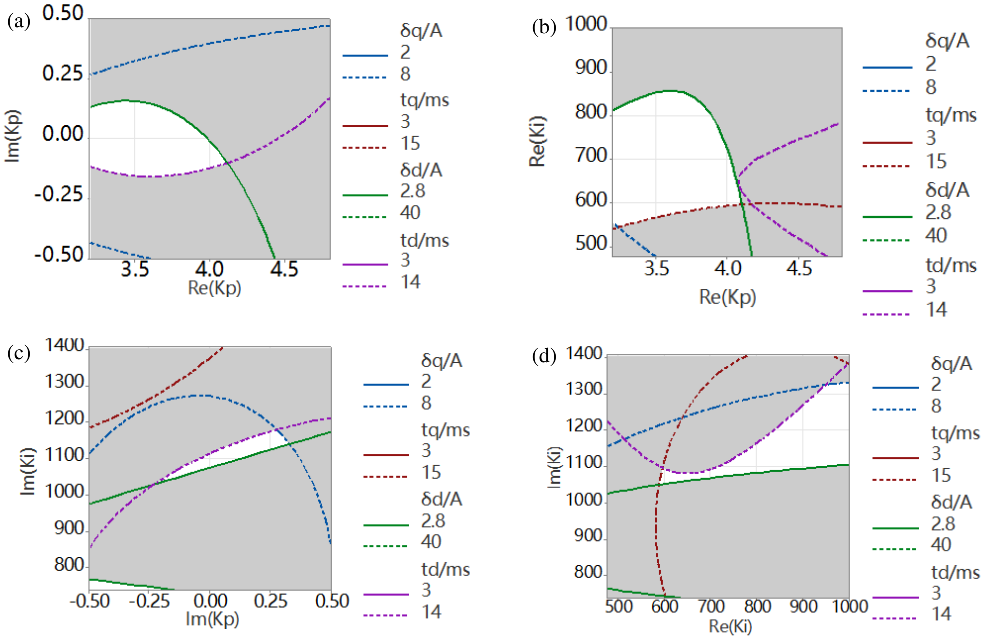

FIGURE 6. Superimposed contour maps of t_d, t_q, δ_d, and δ_q.

optimization initial values and parameter boundaries, ensuring that the minimum-value optimization is performed within a feasible region and that results are both reliable and practical.

3.2. PI Parameter Optimization Method

The Generalized Reduced Gradient (GRG) method is an efficient nonlinear programming technique widely used in multivariable constrained optimization problems, and it is equally applicable to the optimization of PI parameters. To ensure that the system achieves shorter settling times and smaller current overshoots in dynamic performance, this paper adopts the weighted sum of four performance indices — $t_d, t_q, \delta_d, \delta_q$ — as the objective function to be minimized.

According to the principle of the GRG method, the optimization objective function can be expressed as:

$$f(x) = w_1 t_d(x) + w_2 t_q(x) + w_3 \delta_d(x) + w_4 \delta_q(x) \tag{6}$$

where w_1, w_2, w_3, and w_4 are the weighting coefficients. Equal weights ($w_1 = w_2 = w_3 = w_4 = 0.25$) are assigned in the objective function. This selection reflects the design philosophy that dynamic speed (settling time) and stability (overshoot) are of equal importance in EV drive systems. Furthermore, balanced weights ensure symmetric performance improvements for both the d-axis and q-axis, preventing performance degradation in one axis while optimizing the other.

The constraints are defined as: $gi_{(x)} \in [gi_{\min}, gi_{\max}]$, $i \in t_d, t_q, \delta_d, \delta_q$, which means that the four performance indices must remain within the predefined acceptable ranges: $\delta_q \in [2, 8]$, $t_q \in [3, 15]$, $\delta_d \in [2.8, 40]$, $t_d \in [3, 14]$.

Based on the GRG method, the gradient of the objective function $f(x)$ with respect to the controller parameters is given by:

$$\nabla y = \left(\frac{\partial y}{\partial \mathrm{Re}(K_p)}, \frac{\partial y}{\partial \mathrm{Im}(K_p)}, \frac{\partial y}{\partial \mathrm{Re}(K_i)}, \frac{\partial y}{\partial \mathrm{Im}(K_i)} \right) \tag{7}$$

Let the initial parameter vector be x_1. After k iterations, the update formula is:

$$x_{k+1} = x_k + \alpha_k p_k \tag{8}$$

where p_k is the descent direction, and α_k is the step size chosen within the range [0, $\alpha_{\max}$] such that $f(x_k + \alpha_k p_k)$ is minimized.

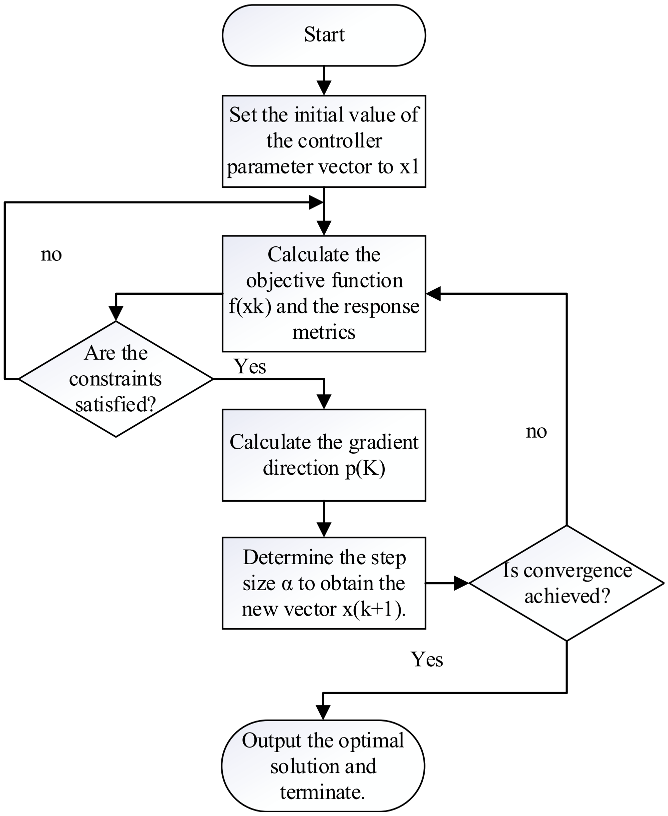

FIGURE 7. Optimization flow of the generalized reduced gradient (GRG) algorithm.

TABLE 6. Comparison of PI parameters and response performance before and after optimization.

Condition	$\mathrm{Re}(K_p)$	$\mathrm{Im}(K_p)$	$\mathrm{Re}(K_i)$	$\mathrm{Im}(K_i)$	td (ms)	δd (A)	tq (ms)	δq (A)
Pre-Optimization	3.2	-0.5	477.1	1405.4	14	8.09	37.95	12.9
DOE Center Point	4	0	739.4	1072.4	13.23	2.8	8.46	6.98
Optimized (GRG)	3.2	-0.21	1001.7	739.4	7.63	0.76	3.57	6.09

Figure 7 illustrates the optimization flowchart of the GRG method. The termination condition is defined as the convergence of $f(x_k)$ to its minimum value. Based on the feasible region identified from the DOE analysis, the optimization search space for the PI controller parameters is constrained within the bounds summarized in Table 1.

The initial parameter vector is selected as: $[\mathrm{Re}(K_p), \mathrm{Im}(K_p), \mathrm{Re}(K_i), \mathrm{Im}(K_i)] = [4, 0, 739.4, 1072.4]$. Through iterative computation of the GRG algorithm, the optimized PI parameters are obtained, ensuring that all four performance indices fall within the acceptable range while minimizing the objective function. Consequently, the system achieves optimal adjustment of its dynamic performance.

The core idea is to iteratively guide the objective function along the descent direction of the gradient to gradually approach the optimum. Starting from the initial parameter vector, the system response is calculated, and constraint satisfaction is checked. If the constraints are satisfied, the gradient information is used to determine the descent direction, and a suitable step size is searched within the feasible region to update the parameter vector. This process repeats until the objective function converges or the preset termination condition is met.

The final parameter set obtained represents the optimal PI controller configuration. Compared with conventional trial-and-error tuning, the GRG method enables comprehensive multi-index optimization under constraints, thereby enhancing the coordination between dynamic and steady-state performance in the complex-vector control system.

Table 6 presents a systematic comparison of the controller parameters and system responses. It is evident that the optimized parameters yield significant improvements, reducing the settling time by approximately 45–90% and the overshoot by over 90% compared to the pre-optimization state.

Regarding the validity of the response surface models, the statistical analysis indicates a high degree of fit. The coefficient of determination (R^2) for all four response models exceeds 0.9, and the adjusted R^2 values are in close agreement, confirming the model's predictive accuracy. The Lack-of-Fit tests yielded p-values greater than 0.05, implying that the quadratic models adequately capture the system dynamics. Furthermore, residual analysis confirms that the residuals follow a normal distribution, validating the statistical assumptions underlying the RSM.

4. SIMULATION AND EXPERIMENTAL VALIDATION

To further verify the effectiveness of the PI controller parameters obtained through response surface optimization, both simulation and practical experiments are conducted for system performance evaluation. By comparing the system responses before and after optimization, the advantages of the proposed method in improving the dynamic characteristics of the current loop are clearly demonstrated. The verification mainly focuses on four aspects: the regulation time and overshoot of active and reactive currents, steady-state accuracy, and system robustness under disturbances or sudden load changes.

4.1. Simulation Model Development

A motor drive control system was built on the MATLAB/Simulink platform, as shown in Figure 8.

4.2. Simulation Validation

To validate the effectiveness of the PI parameter optimization strategy, the performance of the control system was compared under steady-state and dynamic disturbance conditions. Figures 9–12 present the three-phase current waveforms and dq-axis current waveforms before and after optimization.

Under conventional PI control, the three-phase currents are approximately sinusoidal but still show slight distortion. After optimization, the waveforms become smoother and closer to the ideal sinusoidal shape, while the overshoot is significantly reduced. This demonstrates that the optimized parameters effectively suppress output current harmonics.

In steady state, the dq-axis currents under conventional PI control exhibit noticeable ripples, whereas the optimized waveforms are flatter with suppressed ripple components. This indicates that the optimized PI parameters bring higher steady-state accuracy and improved disturbance rejection.

The comparison clearly illustrates a leap in dynamic performance. Under conventional PI control, the system response shows large overshoot, long settling times, and even oscillations. After optimization, the response becomes faster and monotonic, almost free of overshoot, with significantly shorter transient duration and enhanced robustness.

Under conventional PI control, the active current response of the system was relatively slow, exhibiting noticeable delay and overshoot, and the steady-state establishment process was prolonged. After parameter optimization, the current response speed was significantly improved; the adjustment process became smoother; and the system could quickly converge to the steady state with a markedly reduced overshoot. The dynamic performance of the reactive current was also greatly enhanced; after optimization, the response became faster, the overshoot was substantially weakened, and both the transient regulation capability and dynamic stability of the system were effectively improved. These results demonstrate the remarkable effective-

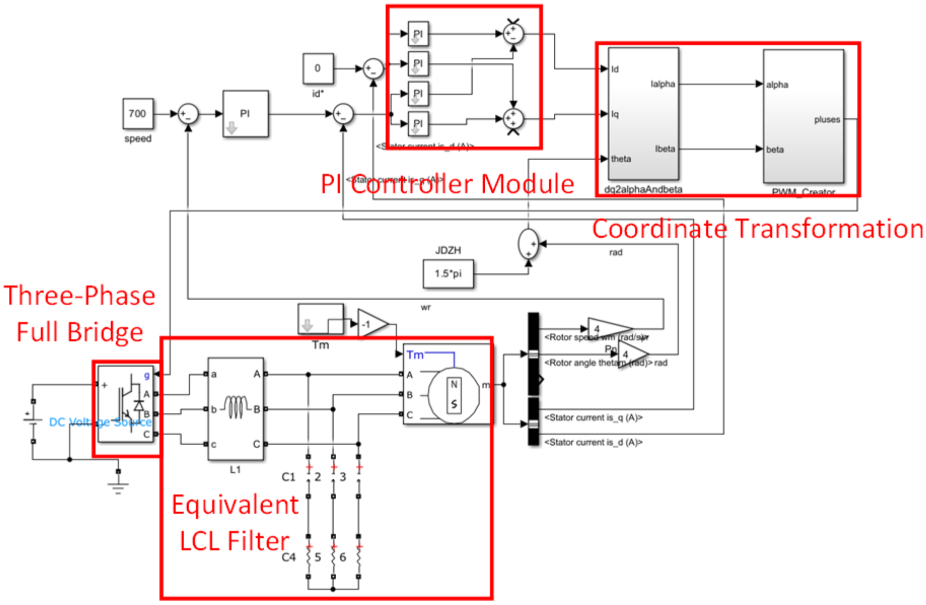

FIGURE 8. Simulink model of the current loop in an EV drive motor controller.

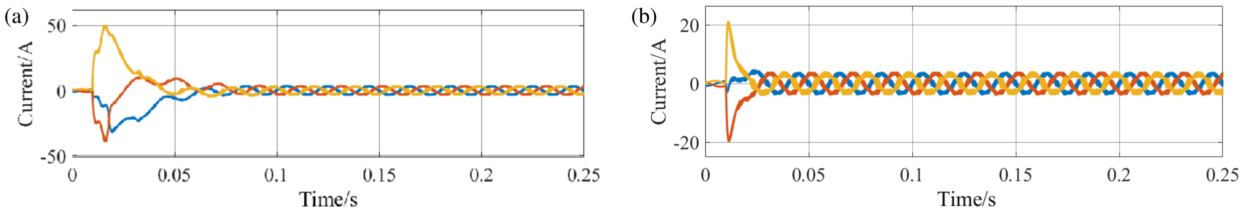

FIGURE 9. Comparison of steady-state three-phase current waveforms before and after PI parameter optimization.

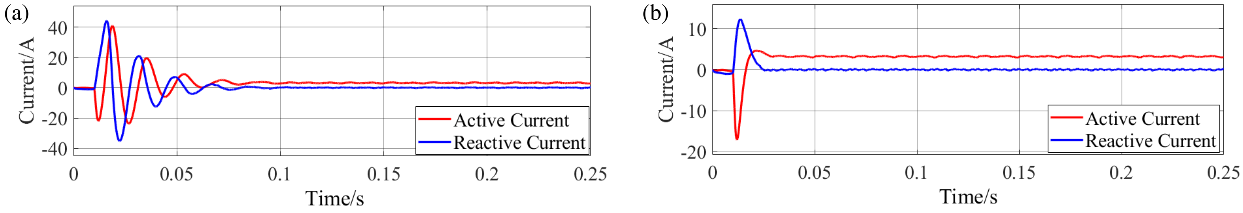

FIGURE 10. Comparison of steady-state dq-axis current waveforms before and after PI parameter optimization.

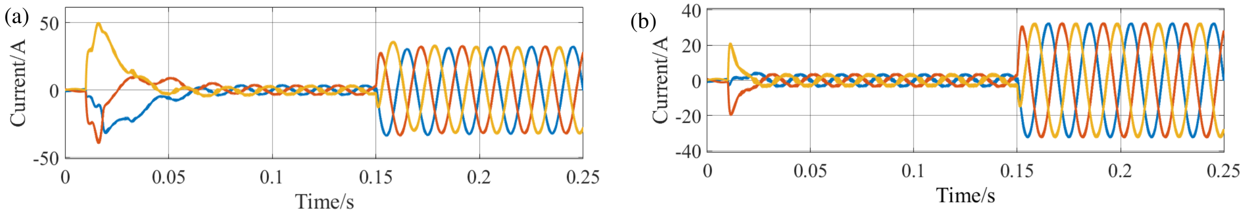

FIGURE 11. Comparison of dynamic responses of three-phase currents under sudden current changes before and after optimization.

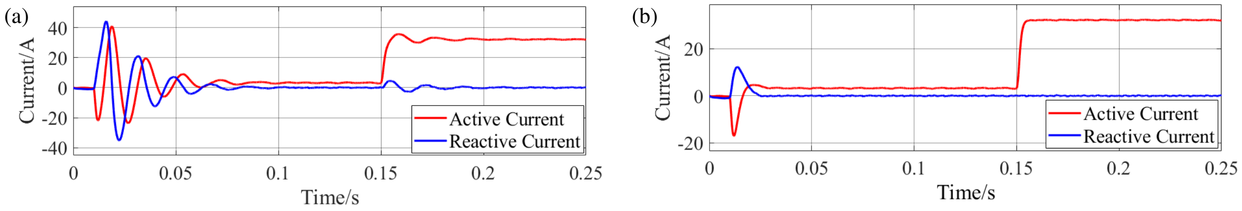

FIGURE 12. Comparison of dq-axis current dynamic responses under sudden changes before and after optimization.

TABLE 7. Quantitative comparison of simulation performance indices.

Performance Metric	Conventional PI	Optimized Complex PI	Improvement
t_q	37.95 ms	3.57 ms	90.6%
δ_q	12.90 A	6.09 A	52.8%
t_d	14.00 ms	7.63 ms	45.5%
δ_d	8.09 A	0.76 A	90.60%
Phase Current THD	5.19%	2.42%	53.40%
Steady-State Current Ripple	1.00 A	0.47 A	53.0%

TABLE 8. Key parameters of the experimental PMSM drive system.

Category	Parameter	Symbol	Value
PMSM	Rated Power	P_n	6.0 kW
	Rated Speed	n_n	3000 rpm
	Rated Torque	T_n	19.1 Nm
	Rated Current	I_n	12.5 A
	Pole Pairs	p	4
	Stator Resistance	R_s	0.35
	d-axis Inductance	L_d	3.5 mH
	q-axis Inductance	L_q	3.5 mH
	Flux Linkage	ψ_f	0.12 Wb
LCL Filter	Inverter-side Inductance	L_1	1.0 mH
	Filter Capacitance	C_f	10 µF
Controller	DC Bus Voltage	U_{dc}	540 V
	Switching Frequency	f_{sw}	10 kHz
	Sampling Frequency	f_s	10 kHz
	Control Unit	DSP	TMS320F28335
	Clock Frequency	f_{clk}	150 MHz
	Encoder Resolution	-	2500 lines

ness of the optimized control strategy in enhancing the performance of the current loop.

To quantitatively evaluate the overall performance improvement, the key simulation indices are summarized in Table 7. Compared with the conventional PI controller, the optimized complex vector PI controller reduces the settling time by over 45% and suppresses the current overshoot by up to 90%. Furthermore, the steady-state performance is significantly enhanced, with the Total Harmonic Distortion (THD) reduced from 5.19% to 2.42% and the current ripple suppressed from 1.00 A to 0.47 A, validating the effectiveness of the proposed harmonic suppression strategy.

4.3. Experimental Validation

To verify the effectiveness of the proposed complex-vector-based PI parameter optimization method in practical systems, a dynamic performance verification test was conducted on the built PMSM drive test platform. The experimental validation was conducted on a high-performance motor drive test bench. The detailed specifications of the PMSM, LCL filter, and control system are listed in Table 8. The main control unit adopts a TI TMS320F28335 DSP with a clock frequency of 150 MHz. The switching frequency and sampling frequency are both set to 10 kHz. The DC bus voltage is stabilized at 540 V.

As mentioned in the performance comparison, the experimental operating conditions were configured to represent a typical severe load disturbance scenario: the motor was controlled to run at the rated speed of 3000 rpm, and a step load of 20 Nm was applied to verify the system robustness.

The overall logical structure of the test bench is shown in Figure 13, which mainly consists of a DC power supply, driver board, main control board (TMS320F28335), LCL filter, PMSM test rig, torque and power analyzer, and oscilloscope.

In this setup, the DC power supply provides a stable DC-link voltage for the inverter; the driver board amplifies SVPWM signals to drive the three-phase bridge; the control board (TMS320F28335) executes the PI current loop algorithm, performs dq-coordinate transformation, and generates SVPWM signals. The torque and power analyzer measures the real-time speed and output torque of the motor, while the oscilloscope captures the current waveforms and evaluates the dynamic response characteristics. All measurement signals are

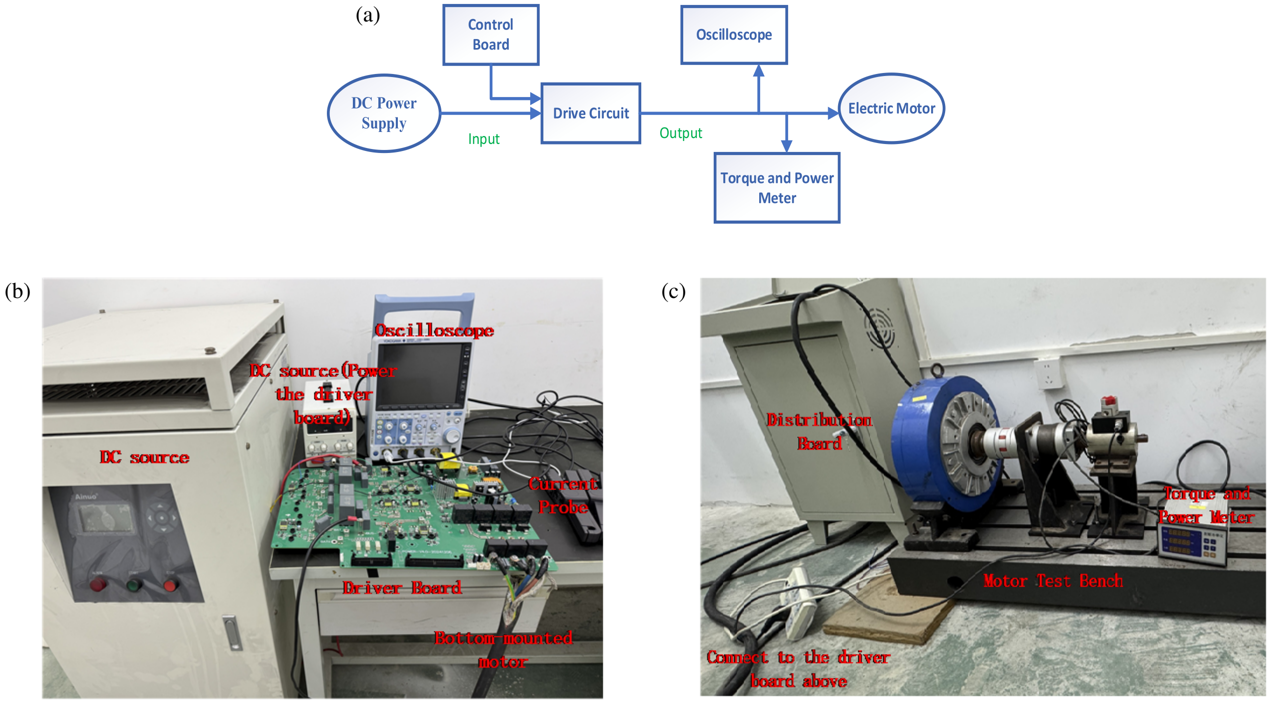

FIGURE 13. Test platform.

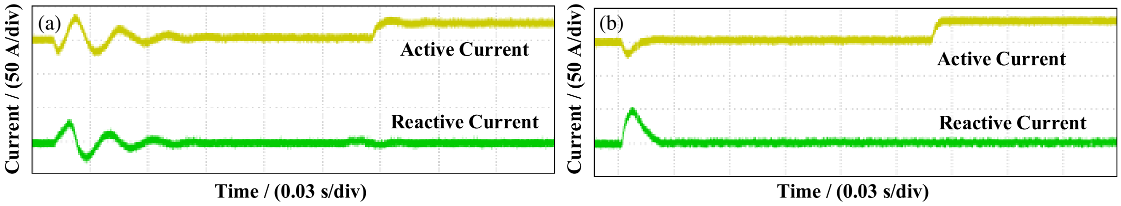

FIGURE 14. Dynamic response of active and reactive currents.

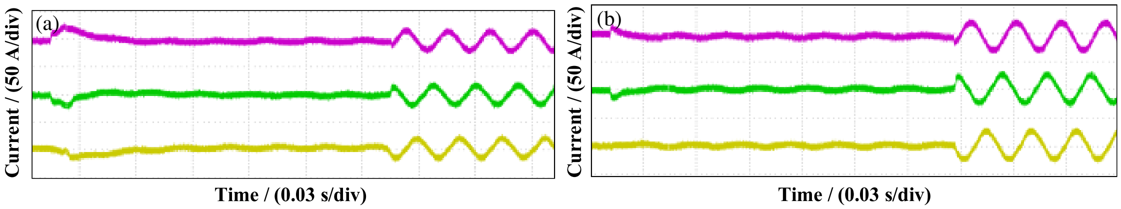

FIGURE 15. Three-phase current waveforms.

transmitted through isolated and high-speed sampling circuits to ensure both accuracy and safety of the test data.

First, a current step experiment was conducted under the non-optimized PI parameters to observe the system response to a step current command. The waveforms of the active current (I_d) and reactive current (I_q) under conventional PI control are shown in Figure 14(a). It can be observed that the response exhibits significant overshoot and oscillation, with a long settling time, indicating a dynamic lag phenomenon caused by parameter mismatch in the controller.

Subsequently, the controller was retuned using the complex-coefficient PI parameters obtained from response surface optimization, and the same test was repeated under identical conditions. The optimized active and reactive current responses are shown in Figure 14(b). The results show that the optimized system can quickly track the reference changes with a smooth rising edge and almost no overshoot. The response time is reduced by approximately 50%, indicating a remarkable improvement in dynamic performance.

To further verify the controller's dynamic robustness, the three-phase current waveforms of the system before and after optimization were recorded, as shown in Figures 15(a) and (b). Under conventional PI control, the three-phase currents exhibit noticeable distortion and phase asymmetry, while after optimization, the current waveforms are nearly ideal sine waves with consistent amplitudes and precise 120° phase separation.

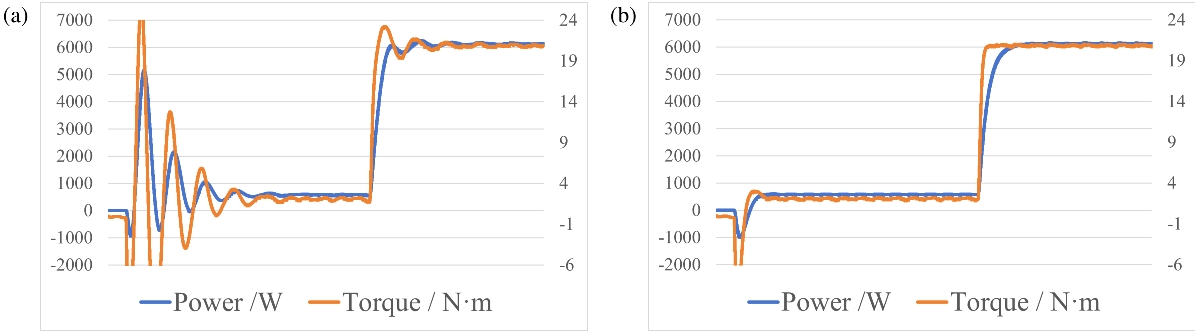

FIGURE 16. Comparison of torque and power variation curves.

TABLE 9. Experimental performance comparison under rated speed and load step conditions.

Performance Metric	Conventional PI	Optimized Complex PI	Note
Current Rise Time	6.2 ms	3.1 ms	50.00%
Current Settling Time	14.5 ms	7.6 ms	47.60%
Current Overshoot	12.50%	0.80%	Eliminated
Torque Overshoot	4.2 Nm	0.3 Nm	92.80%
Output Power Fluctuation	±450 W	±60 W	86.70%

This demonstrates that the optimized parameters effectively suppress current coupling and improve dynamic balance.

To further verify the influence of PI parameter optimization on the system's electromagnetic performance, the variations of motor torque and output power before and after optimization were recorded, as shown in Figure 16.

Figure 16(a) presents the pre-optimization results, where the torque exhibits significant overshoot and oscillation during the step response, and the power curve shows transient fluctuations. In contrast, Figure 16(b) shows the post-optimization results, where the torque responds rapidly and smoothly to command changes, and the power output becomes more stable. This indicates that the optimized PI parameters effectively enhance the system's dynamic energy transfer capability and control precision.

To provide a comprehensive quantitative assessment of the proposed method under the tested operating conditions (3000 rpm, 20 Nm step), the key performance indicators are summarized in Table 9. Compared to the conventional PI controller, the optimized strategy reduces the current rise time by approximately 50% and the settling time by over 47%. Most notably, the current overshoot is practically eliminated (reduced from 12.5% to 0.8%). Furthermore, the mechanical impact is significantly mitigated, with torque overshoot reduced by 92.8% and steady-state power fluctuation suppressed by 86.7%, confirming the superior dynamic robustness of the proposed control scheme.

5. CONCLUSION

This paper proposes a complex-vector-based PI parameter optimization method to address current loop coupling and dynamic degradation in LCL-filtered PMSM drives. First, a frequency-domain complex-vector model was established to transform a MIMO system into an equivalent SISO model, explicitly revealing the LCL coupling mechanism. Accordingly, a complex-coefficient PI controller with decoupling compensation was designed. Second, a systematic optimization framework combining Central Composite Design (CCD)-based Response Surface Methodology (RSM) and the Generalized Reduced Gradient (GRG) algorithm was implemented to balance conflicting dynamic indices.

Experimental results verify the method's effectiveness. Quantitatively, the experimental results under rated load step conditions show that the current settling time is reduced from 14.5 ms to 7.6 ms (47.6% reduction), and the torque overshoot is suppressed by 92.8% (from 4.2 Nm to 0.3 Nm). Furthermore, steady-state power fluctuation is mitigated by 86.7%. These improvements confirm that the framework successfully mitigates the tradeoff between response speed and stability while maintaining high consistency between simulation and implementation.

In conclusion, the proposed method simplifies the modeling of complex PMSM systems and provides an effective optimization path for EV drive systems. Future work will focus on integrating online parameter identification and adaptive control to enhance system adaptability.

REFERENCES

[1] Ren, X., "New energy vehicles and motor drive control technology," *Automation Application*, No. 5, 95–97, 2022.

[2] Zhang, B., Z. Song, S. Liu, R. Huang, and C. Liu, "Overview of integrated electric motor drives: Opportunities and challenges," *Energies*, Vol. 15, No. 21, 8299, 2022.

[3] Zhou, J., G. Xu, X. Zhao, *et al.*, "Optimization design of strong robust controller for an LCL-type active power filter," *Power System Protection and Control*, Vol. 50, No. 10, 140–152, 2022.

[4] Liu, H., X. Bian, W. Zhang, *et al.*, "Novel capacitor current feedback active damping strategy for extending the range of equivalent virtual damping," *High Voltage Engineering*, Vol. 48, No. 1, 114–124, 2022.

[5] Zhang, J. and M. Wang, "Passive damping control strategy of LCL-type PV grid-connected inverter," *Chinese Journal of Power Sources (or Dianyuan Jishu)*, Vol. 44, No. 9, 1334–1337, 2020 (in Chinese).

[6] Li, J., X. Wu, J. Yi, *et al.*, "Improved control strategy of LCL in-verter with double closed-loop state feedback," *Power Electronics (or Power Electronics Technology/Dianli Dianzi Jishu)*, Vol. 51, No. 9, 68–70, 2017 (in Chinese).

[7] Xu, J., L. Ji, X. Ge, *et al.*, "LCL-filter optimization design with consideration of inverter-side current feedback control impacts," *Proceedings of the CSEE*, Vol. 36, No. 17, 4656–4664, 2016.

[8] Li, Y., F. Wang, S. Yang, *et al.*, "Research on vector control strategy of open-end permanent magnet synchronous motor drive based on common mode connected dc buses with a floating bridge," *Proceedings of the CSEE*, Vol. 42, No. 13, 4942–4954, 2022.

[9] Miao, J., X. Li, and B. Dong, "Vector control strategy of permanent magnet synchronous motor based on model reference adaptive," *Mechanical Engineering & Automation*, No. 6, 16–18, 2020.

[10] Yi, L., Y. Wang, W. Li, *et al.*, "Improved monkey algorithm optimizes ADRC vector control strategy of PMSM," *Transducer and Microsystem Technologies*, Vol. 41, No. 11, 52–56, 2022.

[11] Yin, Z., D. Zhang, J. Cai, *et al.*, "A vector control method based on three-degree-of-freedom internal model control for permanent magnet synchronous motor," *Transactions of China Electrotechnical Society*, Vol. 32, No. 21, 55–64, 2017.

[12] Xu, D. and Z. Zhang, "An improved dual-vector model predictive control strategy for permanent magnet synchronous motor," *Electric Machines & Control Application*, Vol. 49, No. 11, 1–8, 2022.

[13] Yao, J., R. Liu, and X. Yin, "Research on 3-vector model predictive control with low switching frequency of permanent magnet synchronous motor," *Transactions of China Electrotechnical Society*, Vol. 33, No. 13, 2935–2945, 2018.

[14] Bao, F., H. Guo, Y. Liu, *et al.*, "Dynamic performance improvement strategy of current loop based on complex vector decoupling," *Micromotors (or Weidianji)*, Vol. 52, No. 12, 74–80, 2019 (in Chinese).

[15] Zhang, H., F. Chen, G. Chen, *et al.*, "Low carrier ratio optimized complex vector control for PMSM," *Micromotors (or Weidianji)*, Vol. 54, No. 8, 62–67, 2021 (in Chinese).

[16] Xu, G., F. Xiao, C. Lian, *et al.*, "A vector control strategy using a single current sensor for a three-phase permanent magnet synchronous motor," *Power System Protection and Control*, Vol. 50, No. 23, 104–111, 2022.

[17] Qu, K., W. Li, T. Ye, *et al.*, "State feedback based decoupling control strategy for grid-connected inverter with LCL filter," *Transactions of China Electrotechnical Society*, Vol. 31, No. 20, 130–138, 2016.

[18] Peng, Q., H. Pan, Y. Liu, *et al.*, "Design of dual-loop decoupling controller in LCL three-phase grid-connected inverter," *Transactions of China Electrotechnical Society*, Vol. 29, No. 4, 103–110, 2014.

[19] Huang, Y., X. Jiang, and A. Qiu, "Active damping control of three-phase rectifier with LCL-filter," *Electric Power Automation Equipment*, Vol. 29, No. 2, 26–29, 2009.

[20] Harnefors, L., "Modeling of three-phase dynamic systems using complex transfer functions and transfer matrices," *IEEE Transactions on Industrial Electronics*, Vol. 54, No. 4, 2239–2248, 2007.

[21] Lyu, Z. and L. Wu, "Current control scheme for LC-equipped PMSM drive considering decoupling and resonance suppression in synchronous complex-vector frame," *IEEE Journal of Emerging and Selected Topics in Power Electronics*, Vol. 11, No. 2, 2061–2073, 2023.

[22] Du, J., H. Li, X. Xiang, B. Yuan, and P. Jiang, "Surrogate model-based full operating condition optimization design for permanent magnet synchronous motors," in *2025 IEEE International Conference on Electrical Energy Conversion Systems and Control (IEECSC)*, 41–47, Chongqing, China, 2025.

[23] Cheng, C., L. Shi, M. Hu, W. Hua, and Y. Hu, "Robust fast current control for LCL-equipped high-speed PMSMs with reduced delay," *IEEE Transactions on Transportation Electrification*, Vol. 11, No. 1, 3896–3906, 2025.

[24] Harnefors, L., A. G. Yepes, A. Vidal, and J. Doval-Gandoy, "Passivity-based controller design of grid-connected VSCs for prevention of electrical resonance instability," *IEEE Transactions on Industrial Electronics*, Vol. 62, No. 2, 702–710, 2015.

[25] Liu, X., Y. Li, L. Xia, X. Tan, and X. Cao, "Research on permanent magnet synchronous motor algorithm based on linear nonlinear switching self-disturbance rejection control," *Scientific Reports*, Vol. 13, No. 1, 20133, 2023.